Supporting Information

Multifunctional inorganic nanomaterials for energy applications

Huilin Wang,[a,b] Xitong Liang,[a,b] Jiutian Wang,[a,b] Shengjian Jiao[a,b]
and Dongfeng Xue*[a,b]

*Corresponding author: E-mail: dongfeng@ciac.ac.cn

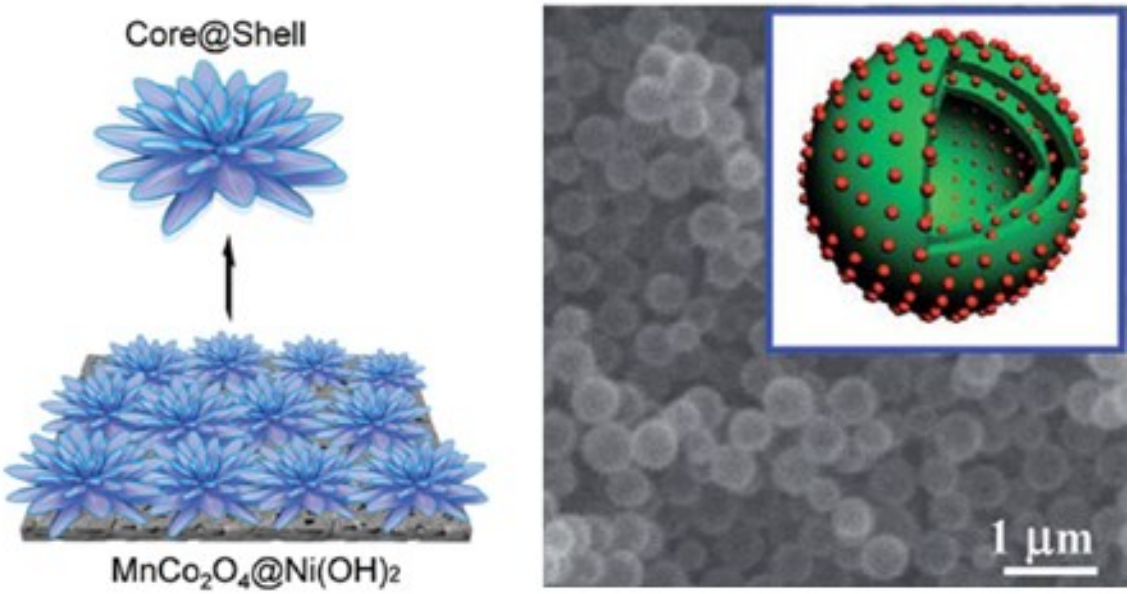

Fig. S1 $MnCo_2O_4$@$Ni(OH)_2$ core-shell flowers for asymmetric supercapacitor materials with ultrahigh specific capacitance and V_2O_5–SnO_2 double-shelled nanospheres. [1, 2]

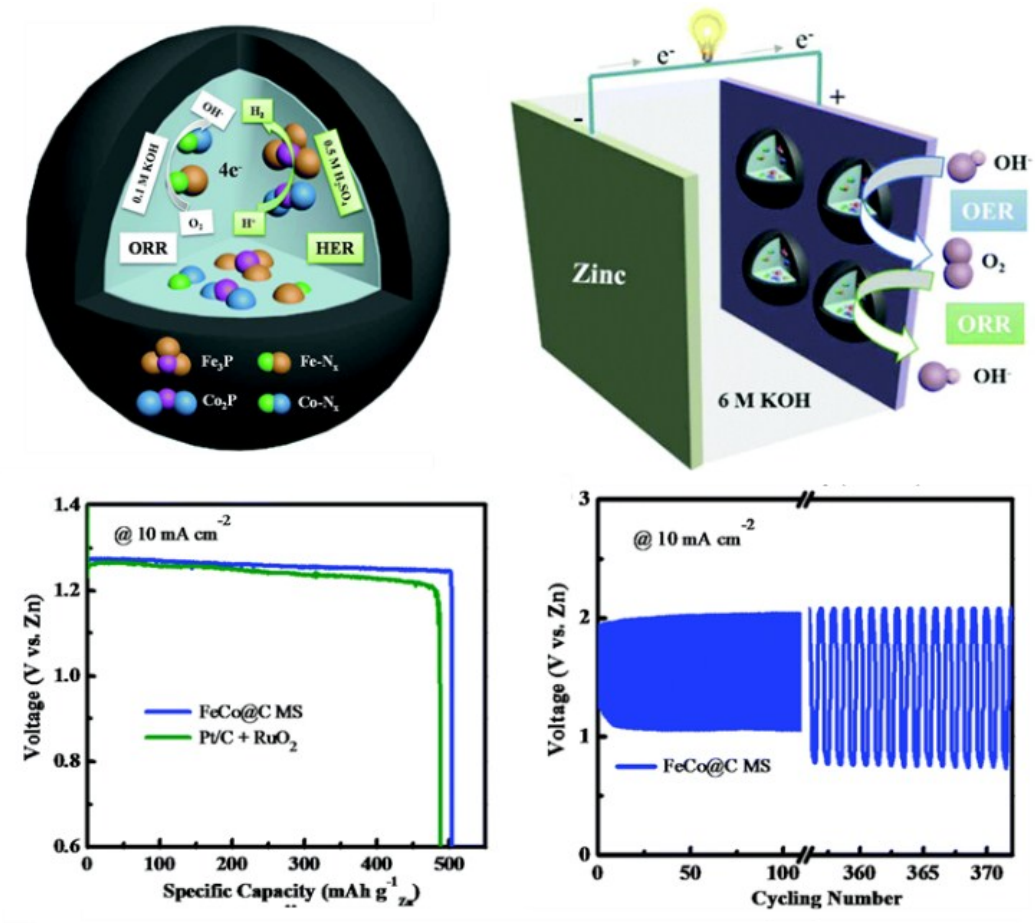

Fig. S2 (a) Schematic illustration of ORR and HER processes of FeCo@C MS. (b) Illustration of the rechargeable Zn–air battery. (c) Electrochemical performance of rechargeable Zn–air batteries using FeCo@C MS as catalysts in 6 M KOH. Galvanostatic discharge curves of primary Zn–air batteries. The specific capacity is normalized by the mass of the consumed Zn anode. (d) Pulse cycling performance of the rechargeable Zn–air batteries using FeCo@C MS at 10 mA cm^{-2} with 5 min discharge and 5 min charge. [3]

Table S1 Summaries of performance and preparation of multifunctional inorganic materials in various energy applications

	Material	Morphology	Application	Performance	Preparation	Reference
Energy generation	SnSe	Nanosheet	Thermoelectric	Low thermal conductivity High ZT of 0.055 at 501 K	Thermal evaporation	4
	Cd-doped SnSe	Nano-crystal	Thermoelectric	Low thermal conductivity High power factor High hole carrier concentration High ZT approximate to 1.7 at 823 K	Solvothermal	5
	$Sn_{0.99}Na_{0.01}Se$-STSe	Nanoprecipitate	Thermoelectric	Ultralow lattice thermal conductivity of below 0.3 W m^{-1} K^{-1} High peak ZT of 1.33 at 773 K	High temperature melting	6
	PbTe-4% InSb	Nanocomposite	Thermoelectric	High ZT of 1.83 at 773 K	High pressure heat treatment	7
	Cu_5FeS_4	Core-shell	Thermoelectric	High power factor Low thermal conductivity Enhanced ZT value of ≈0.62 at 710 K	Colloidal synthesis	8
	Cu_2Se/CNT	Nanocomposite	Thermoelectric	Low lattice thermal conductivity Record-high ZT of 2.4 at 1000 K	High energy ball-milling	9
	C_{60}/TiS_2	Nanocomposite	Thermoelectric	Flexible High Seebeck coefficient High power factor	Printing	10

				High ZT approximate to 0.3 at 400 K		
	Kevlar microfiber-ZnO	Nanowire	Piezoelectric	High flexibility Robustness and durability Open-circuit voltage and short-circuit current are 1.8 mV and 4.8 pA, respectively.	Solvothermal	11
	S-treated MoS_2	Nanosheet	Piezoelectric	Output peak current and voltage are increased by more than 3 times (100 pA) and 2 times (22 mV), respectively.	Chemical vapor deposition	12
	PVDF-AgNW	Nanofiber	Triboelectric	Excellent mechanical stability High output performances	Electrospinning	13
	P(VDF-TrFE)	Nanocomposite	Triboelectric	Boosting power-generating performance is achieved for 1130 V of output voltage and 1.5 mA of output current	Spin-coating heat treatment	14
	Al/PTFE	Micro-nanocomposite	Triboelectric	Excellent high-temperature tolerance (temperature ring of -30 to 550 °C) Wear-resisting ability High hardness (rockwell hardness: 63 HRM) High output voltage and current of 221 V and 27.9 μA cm^{-2}	Ball-milling	15
Energy conversion	$ZnO-SnO_2$	Core-shell	Solar cell	PCE：14.35% Good match between the energy level of the SnO_2 shell High electron mobility of the core ZnO nanoparticles	Coprecipitation	16
	TiO_2–SiO_2	Core-shell	Solar cell	PCE：7.00% Anti-reflective coating decrease the reflectance by producing a refractive index gradient	E-beam evaporation and chemical bath deposition	17

	n-ZnO/p-SnS	Core–shell nanowire array	Solar cell	Relative conversion efficiency：37.3% The piezo-phototronic effect was effectively applied to improve The relative conversion efficiency	Rf magnetron sputtering	18
	PbS–CdS	Core–shell quantum dot	Solar cell	PCE：2.5% Improved passivation of the PbS Surface by the CdS shell, leading to a lower electron trap density	Hot injection	19
	WO_3–TiO_2	Core–shell	Solar cell	PCE：11.24% WO_3 nanosheet arrays yield significantly enhanced photovoltaic performance as compared to nanoparticles and nanorod arrays Due to good perovskite absorber infiltration in the porous scaffold and more rapid carrier transport.	Electrospraying and hydrothermal	20
	PbSe-PbS	Core-shell quantum dot	Solar cell	PCE: 6.5% PbS shell formation on the PbSe core mitigates the trade-off relationship between the open circuit voltage and the short circuit current density.	Precipitation	21
	Pt–C	Core–shell	Fuel cell	A negligible voltage loss after 30000 cycles The robustness of the carbon shells that secure the Pt nanoparticles.	Ultrasonic mixing and heat treatment	22
	IrNi@PdIr/C	Core–shell	Fuel cell	Specific activity is 2.2 times that of commercial Pt/C PdIr shell inhibits oxide formation.	Replacement reaction	23
	Pd/PtCu	Core–shell	Fuel cell	ORR and MOR mass activities were 8.3 and 3.3 times higher than those of commercial Pt, respectively	One-pot epitaxial growth	24

				Lower the catalyst cost but also improve the catalytic activity and stability		
	Pt-Rh_xS_y	Core–shell	Fuel cell	Electrochemical active surface area/mass of core-shell catalyst is 7 times that of commercial Rh_xS_y catalyst.	Precipitate and thermal treatment	25
	CNT/Ni	□	Fuel cell	The functionalized redox nanomaterial exhibits reversible electrocatalytic activity for the $H_2/2H^+$ interconversion from pH 0 to 9, with catalytic preference for H_2 oxidation at all pH values.	-	26
	Co_9S_8/MoS_2	Core-shell	Catalysis	HER: 97 mV (10 mA cm^{-2}) Tafel slope: 71 mV dec^{-1} Precisely tune Tensile surface strain	S vapor-assisted	27
	CoP@PS	Core-shell	Catalysis	Her: 80 mV (10 mA cm^{-2}) The significant enhancing effect from nanometer thick amorphous PS layer on the turnover process	Wet chemical process and phosphidation	28
	PtPb/Pt	Core-shell	Catalysis	50,000 voltage cycles with negligible activity decay	Nonaqueous conditions	29
Energy storage	crystallineFe_2O_3/ amorphous Fe2O3	Core-shell nanorod	Supercapacitors	Capacitance of 701 F g^{-1} The tunable amorphous Layer facilitates the Li^+ diffusion while introduced oxygen defects in Fe_2O_3 can be effectively tuned to improve electronic conductivity	Hydrothermal and heat treatment	30
	P-doped $Ni(OH)_2$-MnO_2		Supercapacitors	Areal capacitance of 5.75 F cm^{-2} Without capacitance loss at after 10 000 cycles	Hydrothermal	31

				Large surface area, good mechanical stability High ion diffusivity and numerous electroactive sites		
	Zinc−nickel-cobalt oxide @$Ni(OH)_2$	Core−shell nanowire arrays	Supercapacitors	Specific capacitance of 2847.5 F cm^{-3} (10.678 F cm^{-2}) The increased electrical conductivity of the core electrode	Hydrothermal and calcination	32
	Co_3O_4@$NiCo_2O_4$	Core-shell	Supercapacitors	Specific capacitance of 1450 F g^{-1} Cycling stability (~4.2% loss after 6000 cycles) Rational design of $nico_2o_4$ nanoflakes adhering on Co_3O_4 nanowires, which promotes two electroactive materials utilizing the synergistic effect to supply more pathways for accelerating fast electron and ion transfer	Hydrothermal	33
	Ni-Co@Ni-Co LDH	Core-shell	Supercapacitors	Capacitance of 2200 F g^{-1} 98.9 % after 5000 cycles A novel hierarchical nanotube array with a massive layered top and discretely separated nanotubes in a core–shell structure	Template assisted electrodeposition	34
	$MnCo_2O_4$@$Ni(OH)_2$	Core–shell flowers	Supercapacitors	Capacitance of 2154 F g^{-1} Hierarchical structure can not only efficiently ensure the synergetic effect of the two pseudocapacitive materials but also promote the diffusion and migration of electrolyte ions during the rapid charge/discharge process	Hydrothermal	1
	ErOOH	Colloid	Supercapacitors	Capacitance of 1811 F g^{-1} Short ion diffusion and electron transfer length to enable the fast and	In situ coprecipitation	35

				reversible faradaic reactions		
	V_2O_5–SnO_2	Core-shell	Lithium-ion batteries	Anode: 947 mA h g^{-1} Cathode: 174 mA h g^{-1} The current nanoarchitecture provides short li ion pathways and high electronic and ionic conductivity, and the hollow architecture is able to accommodate large volume variations	Coprecipitation	2
	$Mn_{1-x}Fe_xP$	Solid solution phosphide	Lithium-ion batteries	A capacity of 360 mA h g^{-1} after 100 cycles at a high current density of 2 A g^{-1}	High energy mechanical milling	36
	Cu_3Si-Si@C@G	Core-shell	Lithium-ion batteries	Good rate performance and delivers reversible capacity of 483 mA h g^{-1} after 500 cycles with capacity retention of about 80% at high current density of 4 A g^{-1}	Sol–gel coating	37
	H-MoP@rGO	Core-shell	Sodium-ion batteries	The specific capacity is as high as 353.8 mA h g^{-1} at 1 A g^{-1} after 600 cycles Extraordinary rate performance of 183.4 mA h g^{-1} at an ultrahigh current density of 10 A g^{-1} even after 3000 cycles.	Hydrothermal followed by phosphorization procedure	38
	FeS_2	Foam-like nanostructure	Sodium-ion batteries	High electrical conductivity Good ion diffusion kinetics High inhibition capacity of volume expansion. High capacity of 823 mA h g^{-1} at 0.1 A g^{-1}, very close to the theoretical capacity of FeS_2 Good rate capability of 581 mA h g^{-1} at 5.0 A g^{-1} Good cycle ability of 754 mA h g^{-1} at 0.2 A g^{-1} with 97% retention after	Solution combustion followed by heat treatment	39

				80 cycles		
	VS_4	3D self-assembled nanoarchitectures	Sodium-ion batteries	High reversible capacity of 412 mA h g^{-1} at 0.2 A g^{-1} after 230 cycles Capacity of 345 and 293 mA h g^{-1} even at 1.0 and 2.0 A g^{-1}, respectively	Hydrothermal	40
	$Ti_2Nb_2O_9$	Nanosheet	Sodium-ion batteries	High reversible capacity of 250 mA h g^{-1} at 50 mA g^{-1} at a suitable average voltage of approximate to 0.7 V.	Liquid exfoliation combined with thermal dehydration	41
	Ni/PCNFO	Nanofiber	Lithium-sulfur batteries	High electrical conductivity High specific capacity of 1320 mA h g^{-1} Excellent rate capability of 780 mA h g^{-1} Long cycling stability of 910 mA h g^{-1} after 500 cycles at 0.2 C	Electrospinning	42
	3DNG/TiN	Composite	Lithium-sulfur batteries	Ultrahigh areal capacity of 12.0 mA h cm^{-2} at a high current density of 8.03 mA cm^{-2}	Hydrothermal	43
	rGO/GC/S	Composite	Lithium-sulfur batteries	High capacity of 524 mA h g^{-1} after 100 cycles at a current rate of 0.2 C	Low-temperature wet spinning	44
	Fe_3C@N–C	Core-shell	Lithium-sulfur batteries	High capacity of 1351 mA h g^{-1} at 0.1 C Outstanding rate capability and cycling stability	Thermal treatment	45
	Ni-doped CoO	Nanosheet	zinc-air batteries	Excellent performance with a record-high discharge peak power density of 377 mW cm^{-2}, and works stable for >400 h at 5 mA cm^{-2}	Hydrothermal	46
	FeCo@C MS	Core-shell	zinc-air batteries	High discharge voltage of 1.27 V High specific capacity of 503 mA h g^{-1}	Solvothermal followed by two-step	3

				Energy density of 639 W h kg^{-1}	carbonization	
Energy saving	WO_3	Tunneled phosphorus-doped film	Smart window	6.1 s for the colouration speed and 2.5 s for the bleaching speed Colouration efficiency 55.9 cm^2 C^{-1} Higher retention (91.5%) of transmittance modulation after 1000 electrochromic (EC) cycles	Precipitation, anneal, red P ignition	47
	WO_3	Mesoporous film	Smart window	T_c = 1.4 s T_b = 1.1 s 93.1% of the original value after 1000 cycles and 74.6% after 2500 cycles CE value of 79.7 cm^2 C^{-1}	Dip-coating sol–gel	48
	Cs_xWO_3	Nanorod	Smart window	Visible light transmittance reaching 78.22% NIR shielding rate being 97.36% Transparent insulation index attaining 175.58	Solvothermal, heat-treat, citric acid thermolysis	49
	Pt-doped K_xWO_3	Nanorod	Smart window	Visible light transmittance reaching 39.58% NIR shielding rate being 94.75%	Solvothermal	50
	M_xWO_3/ZnO	Nanorod	Smart window	Visible light transmittance reaching 92 % High NIR shielding rate 50% of toxic no gas could be decomposed by composite and relevant film under the irradiation of UV light	Hydrothermal	51
	BN	Nanosheet	Cooling liquids	2.39 W mK^{-1} at 24 vol% loading	Molten alkali-assisted liquid	52
	Graphene	Nanoplatelet	Coolants	The maximum thermal conductivity enhancement of 22.92% is	Sonication	53

				attained for the sample containing 0.1 wt% at a fluid temperature of 45 °C The dynamic viscosity and density are close to those for DI water High stability		
	GO-TiO_2	Nanosheet	Nanolubricant	The film thickness of lubricant with GO-TiO_2 was 28.07 nm	Solvothermal	54
Energy transmission	Al/InAs	Nanowire	Superconductivity	Biasing the junction to $\phi \approx \pi$ reduces the critical field at which the zero-bias peak appears, with respect to $\phi = 0$	Electron beam lithography	55
	Nb/InAs, Al/InAs	Nanowire	Superconductivity	Al/InAs-nanowire/Al junctions comprising an Al electrode separation of 220 nm With no clear Josephson supercurrent was achieved, the measured voltage signal becomes nonlinear around zero bias current	Mbe(molecular beam epitaxy)	56
	InAs/V	Nanowire	Superconductivity	The nanoscale superconducting vanadium had a high out-of-plane critical field BC = 1.8 T, far exceeding the bulk value Devices fabricated from hybrid InAs/vanadium nanowires showed superconducting transitions at T < 4 K	Mbe(molecular beam epitaxy)	57
	$YBa_2Cu_{3-x}Ni_xO_{7-\delta}$	Nanowire	Superconductivity	The T_c values range between 70 and 93.2 K for samples with x = 0.04 to x = 0.00, respectively, where the substitution of Cu with Ni results in a lower T_c	Electrospinning	58
	ABC-TLG/hBN	Hall bar geometry	Superconductivity	1/4-filling Mott insulator with D = −0.54 V nm^{-1} and n = −5.4 × 1011 cm^{-2}. Estimated superconducting T_c of 0.65 K	Dry transfer	59

				At D = −0.17 V nm^{-1}, where only the 1/2-filling Mott state exists, the phase diagram shows no superconductivity even at base temperature		
	Graphene/α-Mo_2C	Nonlayered	Superconductivity	The extracted value of the interface transparency is T ≈ 0.7−0.8, indicating a highly transparent high-quality graphene-2D α-Mo_2C interface in comparison with previous work on graphene hybrid/heterostructure devices with either deposited or stacked superconducting contacts	Chemical vapor deposition	60
	$NbSe_2$	Nanoplate	Superconductivity	Superconductivity transition is observed within the temperature range of 4.60–5.40 K The T_c at zero magnetic field is 5.05 K, slightly lower than that of bulk $NbSe_2$ (~7.2 K) A magnetic field of 3.0 T completely suppresses the superconductivity down to the lowest measured temperature. T_{BKT} ≈ 4.83 K	Chemical vapor deposition	61
	NbC	3D nanowire	Superconductivity	FIBID planar nanowires become superconducting at T_c ≈ 5 K The critical temperature of free-standing 3D nanowires is as high as T_c ≈ 11 K, which is close to the value of bulk NbC.	Focused ion beam direct writing	62
	WC	3D hollow nanowire	Superconductivity	The nanowires become superconducting at 6.4 K and show large critical magnetic field and critical current density resulting from their quasi-one-dimensional superconducting character.	Focused electron beam induced deposition	63
	ZnO	Flower-shaped particle	Insulating	The conductivity decreased with increasing amount (0.1 to 3 wt%) of coated ZnO nanoparticles The addition of 3 wt% C_8-coated ZnO nanoparticles reduced the	Heat treatment	64

				conductivity of the LDPE by 2–3 orders of magnitude		
	MgO	Hexagonal platelet	Insulating	The lowest volume conductivity was ca. 7×10^{16} S m^{-1} for 3 wt% surface coated nanoparticles Uniformly dispersed MgO nanoparticles up to contents as high as 9 wt%, with maintained 10–100 times reduced volume conductivity	Liquid precipitation and heat treatment	65

1. Y. Zhao, L. F. Hu, S. Y. Zhao and L. M. Wu, *Adv. Funct. Mater.*, 2016, **26**, 4085-4093.
2. J. Liu, H. Xia, D. F. Xue and L. Lu, *J. Am. Chem. Soc.*, 2009, **131**, 12086-12087.
3. Y. T. Xu, B. L. Chen, J. Nie and G. P. Ma, *Nanoscale*, 2018, **10**, 17021-17029.
4. M. R. Burton, T. J. Liu, J. McGettrick, S. Mehraban, J. Baker, A. Pockett, T. Watson, O. Fenwick and M. J. Carnie, *Adv. Mater.*, 2018, **30**, 1801357.
5. X. L. Shi, A. Wu, T. L. Feng, K. Zheng, W. D. Liu, Q. Sun, M. Hong, S. T. Pantelides, Z. G. Chen and J. Zou, *Adv. Energy Mater.*, 2019, **9**, 1803242.
6. Y. B. Luo, S. T. Cai, X. Hua, H. J. Chen, Q. H. Liang, C. F. Du, Y. Zheng, J. H. Shen, J. W. Xu, C. Wolverton, V. P. Dravid, Q. Y. Yan and M. G. Kanatzidis, *Adv. Energy Mater.*, 2019, **9**, 1803072.
7. J. Zhang, D. Wu, D. S. He, D. Feng, M. J. Yin, X. Y. Qin and J. Q. He, *Adv. Mater.*, 2017, **29**, 1703148.
8. A. J. Zhang, B. Zhang, W. Lu, D. D. Xie, H. X. Ou, X. D. Han, J. Y. Dai, X. Lu, G. Han, G. Y. Wang and X. Y. Zhou, *Adv. Funct. Mater.*, 2018, **28**, 1705117.
9. R. Nunna, P. F. Qiu, M. J. Yin, H. Y. Chen, R. Hanus, Q. F. Song, T. S. Zhang, M. Y. Chou, M. T. Agne, J. Q. He, G. J. Snyder, X. Shi and L. D. Chen, *Energy Environ. Sci.*, 2017, **10**, 1928-1935.
10. L. M. Wang, Z. M. Zhang, L. X. Geng, T. Y. Yuan, Y. C. Liu, J. C. Guo, L. Fang, J. J. Qiu and S. R. Wang, *Energy Environ. Sci.*, 2018, **11**, 1307-1317.
11. L. Zhang, S. Bai, C. Su, Y. B. Zheng, Y. Qin, C. Xu and Z. L. Wang, *Adv. Funct. Mater.*, 2015, **25**, 5794-5798.
12. S. A. Han, T. H. Kim, S. K. Kim, K. H. Lee, H. J. Park, J. H. Lee and S. W. Kim, *Adv. Mater.*, 2018, **30**, 1800342.
13. S. Cheon, H. Kang, H. Kim, Y. Son, J. Y. Lee, H. J. Shin, S. W. Kim and J. H. Cho, *Adv. Funct. Mater.*, 2018, **28**, 1703778.
14. W. Seung, H. J. Yoon, T. Y. Kim, H. Ryu, J. Kim, J. H. Lee, J. H. Lee, S. Kim, Y. K. Park, Y. J. Park and S. W. Kim, *Adv. Energy Mater.*, 2017, **7**, 1600988.
15. J. Wen, B. D. Chen, W. Tang, T. Jiang, L. P. Zhu, L. Xu, J. Chen, J. J. Shao, K. Han, W. Ma and Z. L. Wang, *Adv. Energy Mater.*, 2018, **8**, 1801898.
16. Z. Li, R. Wang, J. Xue, X. Xing, C. Yu, T. Huang, J. Chu, K.-L. Wang, C. Dong, Z. Wei, Y. Zhao, Z.-K. Wang and Y. Yang, *J. Am. Chem. Soc.*, 2019, **141**, 17610-17616.

17. C. W. Chen, H. W. Tsai, Y. C. Wang, T. Y. Su, C. H. Yang, W. S. Lin, Z. H. Lin, J. S. Huang and Y. L. Chueh, *J. Mater. Chem. A*, 2019, **7**, 11452-11459.
18. L. P. Zhu, L. F. Wang, F. Xue, L. B. Chen, J. Q. Fu, X. L. Feng, T. F. Li and Z. L. Wang, *Adv. Sci.*, 2017, **4**, 1600185.
19. M. J. Speirs, D. M. Balazs, H. H. Fang, L. H. Lai, L. Protesescu, M. V. Kovalenko and M. A. Loi, *J. Mater. Chem. A*, 2015, **3**, 1450-1457.
20. K. Mahmood, B. S. Swain, A. R. Kirmani and A. Amassian, *J. Mater. Chem. A*, 2015, **3**, 9051-9057.
21. H. Choi, J. H. Song, J. Jang, X. D. Mai, S. Kim and S. Jeong, *Nanoscale*, 2015, **7**, 17473-17481.
22. M. Karuppannan, Y. Kim, S. Gok, E. Lee, J. Y. Hwang, J. H. Jang, Y. H. Cho, T. Lim, Y. E. Sung and O. J. Kwon, *Energy Environ. Sci.*, 2019, **12**, 2820-2829.
23. B. W. Qin, H. M. Yu, J. Jia, C. Jun, X. Q. Gao, D. W. Yao, X. Y. Sun, W. Song, B. L. Yi and Z. G. Shao, *Nanoscale*, 2018, **10**, 4872-4881.
24. F. Lin, K. Wang, Y. H. Tang, J. P. Lai, M. C. Lou, M. H. Huang and S. J. Guo, *Chem. Commun.*, 2018, **54**, 1315-1318.
25. Y. C. Li and T. V. Nguyen, *J. Power Sources*, 2018, **382**, 152-159.
26. S. Gentil, N. Lalaoui, A. Dutta, Y. Nedellec, S. Cosnier, W. J. Shaw, V. Artero and A. Le Goff, *Angew. Chem. Int. Edn.*, 2017, **56**, 1845-1849.
27. H. Zhu, G. H. Gao, M. L. Du, J. H. Zhou, K. Wang, W. B. Wu, X. Chen, Y. Li, P. M. Ma, W. F. Dong, F. Duan, M. Q. Chen, G. M. Wu, J. D. Wu, H. T. Yang and S. J. Guo, *Adv. Mater.*, 2018, **30**, 1707301.
28. D. J. Li, J. Kang, H. J. Lee, D. S. Choi, S. H. Koo, B. Han and S. O. Kim, *Adv. Energy Mater.*, 2018, **8**, 1702806.
29. L. Z. Bu, N. Zhang, S. J. Guo, X. Zhang, J. Li, J. L. Yao, T. Wu, G. Lu, J. Y. Ma, D. Su and X. Q. Huang, *Science*, 2016, **354**, 1410-1414.
30. S. Sun, T. Zhai, C. Liang, S. V. Savilov and H. Xia, *Nano Energy*, 2018, **45**, 390-397.
31. K. Z. Li, S. K. Li, F. Z. Huang, X. Y. Yu, Y. Lu, L. Wang, H. Chen and H. Zhang, *Nanoscale*, 2018, **10**, 2524-2532.
32. Q. C. Zhang, W. W. Xu, J. Sun, Z. H. Pan, J. X. Zhao, X. N. Wang, J. Zhang, P. Man, J. B. Guo, Z. Y. Zhou, B. He, Z. X. Zhang, Q. W. Li, Y. G. Zhang, L. Xu and Y. G. Yao, *Nano Lett.*, 2017, **17**, 7552-7560.
33. X. Wu, Z. C. Han, X. Zheng, S. Y. Yao, X. Yang and T. Y. Zhai, *Nano Energy*, 2017, **31**, 410-417.
34. Y. Liu, N. Q. Fu, G. G. Zhang, M. Xu, W. Lu, L. M. Zhou and H. T. Huang, *Adv. Funct. Mater.*, 2017, **27**, 1605307.
35. K. F. Chen and D. F. Xue, *J. Colloid Interface Sci.*, 2014, **430**, 265-271.
36. K. H. Kim, W. S. Kim and S. H. Hong, *Nanoscale*, 2019, **11**, 13494-13501.
37. Z. M. Zheng, H. H. Wu, H. X. Chen, Y. Cheng, Q. B. Zhang, Q. S. Xie, L. S. Wang, K. L. Zhang, M. S. Wang, D. L. Peng and X. C. Zeng, *Nanoscale*, 2018, **10**, 22203-22214.
38. Y. Y. Yin, L. S. Fan, Y. Zhang, N. N. Liu, N. Q. Zhang and K. N. Sun, *Nanoscale*, 2019, **11**, 7129-7134.
39. R. D. Hu, H. A. Zhao, J. L. Zhang, Q. H. Liang, Y. N. Wang, B. L. Guo, R. Dangol, Y. Zheng, Q. Y. Yan and J. W. Zhu, *Nanoscale*, 2019, **11**, 178-184.

40. W. B. Li, J. F. Huang, L. L. Feng, L. Y. Cao and S. W. He, *Nanoscale*, 2018, **10**, 21671-21680.
41. L. F. Shen, Y. Wang, H. F. Lv, S. Q. Chen, P. A. van Aken, X. J. Wu, J. Maier and Y. Yu, *Adv. Mater.*, 2018, **30**, 1804378.
42. Q. Li, J. N. Guo, J. Zhao, C. C. Wang and F. Yan, *Nanoscale*, 2019, **11**, 647-655.
43. Z. H. Li, Q. He, X. Xu, Y. Zhao, X. W. Liu, C. Zhou, D. Ai, L. X. Xia and L. Q. Mai, *Adv. Mater.*, 2018, **30**, 1804089.
44. W. G. Chong, Y. H. Xiao, J. Q. Huang, S. S. Yao, J. Cui, L. Qin, C. Gao and J. K. Kim, *Nanoscale*, 2018, **10**, 21132-21141.
45. H. Zhang, H. Cui, J. Li, Y. Liu, Y. Yang and M. Wang, *Nanoscale*, 2019, DOI: 10.1039/c9nr07388d.
46. Y. J. Li, L. Cui, P. F. Da, K. W. Qiu, W. J. Qin, W. B. Hu, X. W. Du, K. Davey, T. Ling and S. Z. Qiao, *Adv. Mater.*, 2018, **30**, 1804653.
47. K. Bon-Ryul, K. H. Kim and H. J. Ahn, *Nanoscale*, 2019, **11**, 3318-3325.
48. W. Q. Wang, X. L. Wang, X. H. Xia, Z. J. Yao, Y. Zhong and J. P. Tu, *Nanoscale*, 2018, **10**, 8162-8169.
49. J. X. Liu, B. Chen, C. Y. Fan, F. Shi, S. Ran, J. Y. Yang, X. Song and S. H. Liu, *Crystengcomm*, 2018, **20**, 1509-1519.
50. S. Ran, J. X. Liu, F. Shi, C. Y. Fan, B. Chen, H. M. Zhang, L. Yu and S. H. Liu, *Sol. Energy Mater. Sol. Cells*, 2018, **174**, 342-350.
51. X. Y. Wu, J. T. Wang, G. K. Zhang, K. Katsumata, K. Yanagisawa, T. Sato and S. Yin, *Appl. Catal. B-Environ.*, 2017, **201**, 128-136.
52. X. Hou, M. J. Wang, L. Fu, Y. P. Chen, N. Jiang, C. T. Lin, Z. W. Wang and J. H. Yu, *Nanoscale*, 2018, **10**, 13004-13010.
53. R. Sadri, M. Hosseini, S. N. Kazi, S. Bagheri, A. H. Abdelrazek, G. Ahmadi, N. Zubir, R. Ahmad and N. I. Z. Abidin, *J. Colloid Interface Sci.*, 2018, **509**, 140-152.
54. S. N. Du, J. L. Sun and P. Wu, *Carbon*, 2018, **140**, 338-351.
55. A. Fornieri, A. M. Whiticar, F. Setiawan, E. Portoles, A. C. C. Drachmann, A. Keselman, S. Gronin, C. Thomas, T. Wang, R. Kallaher, G. C. Gardner, E. Berg, M. J. Manfra, A. Stern, C. M. Marcus and F. Nichele, *Nature*, 2019, **569**, 89-92.
56. N. A. Gusken, T. Rieger, P. Zellekens, B. Bennemann, E. Neumann, M. I. Lepsa, T. Schapers and D. Grutzmacher, *Nanoscale*, 2017, **9**, 16735-16741.
57. M. Bjergfelt, D. J. Carrad, T. Kanne, M. Aagesen, E. M. Fiordaliso, E. Johnson, B. Shojaei, C. J. Palmstrom, P. Krogstrup, T. S. Jespersen and J. Nygard, *Nanotechnology*, 2019, **30**, 294005.
58. J. C. Bernard, D. A. Modesto, M. S. Medina, A. Zenatti, E. C. Venancio, E. R. Leite, A. J. C. Lanfredi and M. T. Escote, *Mater. Res. Express*, 2019, **6**, 086001.
59. G. Chen, A. L. Sharpe, P. Gallagher, I. T. Rosen, E. J. Fox, L. Jiang, B. Lyu, H. Li, K. Watanabe, T. Taniguchi, J. Jung, Z. Shi, D. Goldhaber-Gordon, Y. Zhang and F. Wang, *Nature*, 2019, DOI: 10.1038/s41586-019-1393-y.
60. C. Xu, S. A. Song, Z. B. Liu, L. Chen, L. B. Wang, D. X. Fan, N. Kang, X. L. Ma, H. M. Cheng and W. C. Ren, *ACS Nano*, 2017, **11**, 5906-5914.
61. Y. C. Zou, Z. G. Chen, E. Z. Zhang, F. X. Xiu, S. Matsumura, L. Yang, M. Hong and J. Zou, *Nanoscale*, 2017, **9**, 16591-16595.
62. F. Porrati, S. Barth, R. Sachser, O. V. Dobrovolskiy, A. Seybert, A. S. Frangakis and M. Huth, *ACS Nano*, 2019, **13**, 6287-6296.

63. R. Cordoba, A. Ibarra, D. Mailly and J. M. De Teresa, *Nano Lett.*, 2018, **18**, 1379-1386.
64. A. M. Pourrahimi, T. A. Hoang, D. M. Liu, L. K. H. Pallon, S. Gubanski, R. T. Olsson, U. W. Gedde and M. S. Hedenqvist, *Adv. Mater.*, 2016, **28**, 8651-8657.
65. L. K. H. Pallon, A. T. Hoang, A. M. Pourrahimi, M. S. Hedenqvist, F. Nilsson, S. Gubanski, U. W. Gedde and R. T. Otsson, *J. Mater. Chem. A*, 2016, **4**, 8590-8601.